REPORT

SOLID-STATE PHYSICS

Anomalously low electronic thermal conductivity in metallic vanadium dioxide

Sangwook Lee,[1,2]* Kedar Hippalgaonkar,[3,4]* Fan Yang,[3,5]* Jiawang Hong,[6,7]* Changhyun Ko,[1] Joonki Suh,[1] Kai Liu,[1,8] Kevin Wang,[1] Jeffrey J. Urban,[5] Xiang Zhang,[3,8,9] Chris Dames,[3,8] Sean A. Hartnoll,[10] Olivier Delaire,[7,11]† Junqiao Wu[1,8]†

In electrically conductive solids, the Wiedemann-Franz law requires the electronic contribution to thermal conductivity to be proportional to electrical conductivity. Violations of the Wiedemann-Franz law are typically an indication of unconventional quasiparticle dynamics, such as inelastic scattering, or hydrodynamic collective motion of charge carriers, typically pronounced only at cryogenic temperatures. We report an order-of-magnitude breakdown of the Wiedemann-Franz law at high temperatures ranging from 240 to 340 kelvin in metallic vanadium dioxide in the vicinity of its metal-insulator transition. Different from previously established mechanisms, the unusually low electronic thermal conductivity is a signature of the absence of quasiparticles in a strongly correlated electron fluid where heat and charge diffuse independently.

In a Fermi liquid, the same quasiparticles that transport charge also carry heat. Therefore, in most normal metals the charge and heat conductivities are related via the Wiedemann-Franz (WF) law: The ratio between the electronic thermal conductivity (κ_e) and the product of electrical conductivity (σ) and absolute temperature (T) is a constant called the Lorenz number, $L = \kappa_e/\sigma T$, typically not very different from the Sommerfeld value $L_0 = (\pi^2/3)(k_B/e)^2 = 2.44 \times 10^{-8}$ W ohm K^{-2} (where k_B is the Boltzmann constant and e is the electron charge). Recently, violations of the WF law have been theoretically predicted (1–4) or experimentally observed (5–13) in some electronic systems. However, with one exception observed in a one-dimensional conductor at room temperature (13), these violations typically occur at cryogenic temperatures and arise from unconventional phases of matter, strong inelastic scattering of quasiparticles, or semimetal physics. Here we report a drastic breakdown of the WF law at high temperatures, with L smaller than L_0 by almost an order of magnitude, in a strongly correlated metal [vanadium dioxide (VO_2)]. The observed anomalously low electronic thermal conductivity is accompanied by an unusually high electronic thermoelectric figure of merit; tungsten (W) doping causes both properties to partially revert to normal values. The violation of the WF law is attributed to the formation of a strongly correlated, incoherent non-Fermi liquid, in which charge and heat are independently transported by distinct diffusive modes at high temperatures rather than carried by long-lived quasiparticles (14, 15).

We observed the effect in the metallic phase of VO_2 in the vicinity of its metal-insulator transition (MIT). VO_2 undergoes the MIT at 340 K, accompanied by a first-order structural phase transition from the monoclinic insulating (I) phase to the tetragonal metallic (M) phase on heating (16). In this work, κ_e is determined by subtracting the phonon (lattice) thermal conductivity (κ_{ph}), obtained by combining first-principles calculations with x-ray scattering measurements, from the measured total thermal conductivity (κ_{tot}). Previously, κ_{tot} of VO_2 has been measured in bulk and thin films with conflicting conclusions. In bulk VO_2, for example, it was reported that κ_{tot} stays constant (17) or decreases very slightly (18) with increasing T across the MIT. Unknown electronic scattering leading to a possible failure of the WF law in VO_2 was alluded to nearly half a century ago (17), but this has not been experimentally or analytically investigated. Recently, however, time-domain thermal reflectance measurements on polycrystalline VO_2 films showed an increase in κ_{tot}, with a magnitude seemingly consistent with the WF law (19). Unlike in those measurements, we use single-crystal VO_2 nanobeams, where the single crystallinity and freestanding configuration in our measurements eliminate extrinsic domain and strain effects. Moreover, our sample geometry ensures that both heat and charge flow in the same path along the nanobeam length direction. This is a crucial condition that, if not satisfied, could result in an erroneous determination of κ_e and assessment of the WF law, especially for VO_2, which has an anisotropic crystal structure. The single-crystal VO_2 nanobeams were grown by the previously reported vapor-transport method (20–22) (see materials and methods, along with figs. S1 and S2). Figure 1A shows a nanobeam bonded to two microfabricated, suspended pads for simultaneous measurements of κ_{tot}, σ, and the Seebeck coefficient (23, 24) (details in materials and methods, as well as figs. S3 and S4). The thermal and electrical contact resistances were determined to be negligible (materials and methods; see also figs. S5 and S6).

The measured κ_{tot} of a representative VO_2 nanobeam is shown in Fig. 1B. Consistent with a previous study on bulk VO_2 (17), our nanobeams exhibit very little change in κ_{tot} across the MIT: $\Delta\kappa_{tot} \sim 0.2$ W/m·K. More than five VO_2 nanobeams with different sizes were measured, and all show $\Delta\kappa_{tot}$ at this level or lower (materials and methods and fig. S8). From the measured σ of the nanobeam across the MIT, the expected electronic thermal conductivity (κ_e^0) for conventional Fermi liquid transport can be calculated, assuming that both phases obey the WF law ($L = L_0$). With σ rising from 4.6×10^3 S/m (I phase) to 8.0×10^5 S/m (M phase) (where 1 S = 1 A/V), κ_e^0 exhibits an abrupt jump from nearly zero to 6.9 W/m·K (Fig. 1B). The measured $\Delta\kappa_{tot}$ is less than 3% of κ_e^0 in the M phase. Considering that κ_e^0 alone in the M phase is already greater than the measured κ_{tot}, application of the WF law would imply an unphysical, negative κ_{ph} in the M phase.

To better understand this anomaly, we determined κ_{ph} in both I and M phases (κ_{ph}^I and κ_{ph}^M) by combining first-principles calculations with measurements (details in materials and methods and fig. S9). As a first step, the phonon dispersions were calculated using density functional theory (DFT), as shown in Fig. 2A for both I and M phases. From these dispersions, both the phonon group velocity and lattice specific heat were obtained for different phonon modes and wave vectors. Next, on the basis of anharmonic (umklapp) phonon scattering in a pure bulk sample, a full first-principles calculation (25) was performed for the phonon relaxation time in the I phase. In this way, a calculated bulk value of $\kappa_{ph}^{I,bulk} = 6.46$ W/m·K was obtained at $T = 340$ K along the rutile-phase c axis (the nanobeam length direction). To evaluate the final nanobeam phonon thermal conductivity (κ_{ph}^I), Matthiessen's rule was then applied to account for

[1]Department of Materials Science and Engineering, University of California, Berkeley, CA 94720, USA. [2]School of Materials Science and Engineering, Kyungpook National University, Daegu 41566, South Korea. [3]Department of Mechanical Engineering, University of California, Berkeley, CA 94720, USA. [4]Institute of Materials Research and Engineering, A*STAR (Agency for Science, Technology and Research), 2 Fusionopolis Way, Innovis, 08-03, 138634 Singapore. [5]The Molecular Foundry, Lawrence Berkeley National Laboratory, Berkeley, CA 94720, USA. [6]School of Aerospace Engineering and Institute of Advanced Structure Technology, Beijing Institute of Technology, Beijing 100081, China. [7]Materials Science and Technology Division, Oak Ridge National Laboratory, Oak Ridge, TN 37831, USA. [8]Materials Sciences Division, LBNL, Berkeley, CA 94720, USA. [9]Department of Physics, King Abdulaziz University, Jeddah 21589, Saudi Arabia. [10]Department of Physics, Stanford University, Stanford, CA 94305, USA. [11]Department of Mechanical Engineering and Materials Science, Duke University, Durham, NC 27708, USA.
*These authors contributed equally to this work. †Corresponding author. Email: wuj@berkeley.edu (J.W.); olivier.delaire@duke.edu (O.D.)

impurity and diffuse boundary scattering of phonons. Using the known rectangular cross section, this boundary scattering (26) reduces κ_{ph}^I from 6.46 W/m·K for the bulk to 6.15 W/m·K for the nanobeam, very close to the experimentally measured value of 5.8 W/m·K (Fig. 1B). The remaining small difference is attributed to scattering from impurities, most probably atomic vacancies as native point defects (supplementary materials).

For the M phase, evaluating the thermal conductivity solely using first-principles calculations is challenging because VO_2 is a strongly correlated electron system that could exhibit both strong electron-electron and electron-phonon interactions (25). In addition, phonon scattering has not been successfully calculated with current theoretical techniques. However, previous ab initio molecular dynamics simulations within the framework of DFT were successful in predicting anharmonically renormalized phonon dispersions in the M phase, which were in good agreement with energy- and momentum-resolved inelastic x-ray scattering (IXS) experiments previously reported in (25). Using these M-phase first-principles phonon dispersions (Fig. 2A) benchmarked against experiments, together with the phonon scattering rates obtained from the IXS measurements (details in materials and methods and fig. S9), we determined $\kappa_{ph}^{M,bulk} = 5.72$ W/m·K (Fig. 2B), a reduction by 13% from $\kappa_{ph}^{I,bulk}$. Note that this value includes umklapp, electron-phonon scattering, and all other possible scattering of phonons in bulk, defect-free VO_2. With this value of $\kappa_{ph}^{M,bulk}$, using the Matthiessen's rule similar to that used in the I phase, the nanobeam κ_{ph}^M for the M phase was obtained. With both boundary and impurity scatterings considered, κ_{ph}^I and κ_{ph}^M for nanobeams become even closer to each other (Fig. 2B). The electronic thermal conductivity in the M phase (κ_e^M) can then be obtained by subtracting the nanobeam value of κ_e^M from the measured κ_{tot}^M. In this way, we obtained $\kappa_e^M = 0.72$ W/m·K and, hence, an effective Lorenz number $L_{eff} = (\kappa_e^M/\kappa_e^0)\cdot L_0 = 0.11 L_0$, corresponding to a suppression of L by nearly an order of magnitude. Although the uncertainty of κ_e^M is high compared with κ_e^M itself (~80%), L_{eff}/L_0 is still low, with an upper bound of less than 0.2.

We now show that this effect can be tuned in W-doped VO_2 ($W_xV_{1-x}O_2$) nanobeams. Tungsten was chosen as the dopant because it is known to lower the MIT temperature (T_{MIT}) by detwisting the V-V bonds in the monoclinic I phase (16). The effects of W doping on thermal and electrical transport over a wide T range are summarized in Fig. 3, A and B. As can be seen from the electrical conductivity curves, T_{MIT} decreases monotonically with the W-doping fraction x at a rate of ~21 K per atomic % (fig. S1), consistent with previous reports (21, 27). The $W_xV_{1-x}O_2$ nanobeams show a clear jump in κ_{tot} across their MIT, accompanying the abrupt jump in σ, in marked contrast to the behavior of undoped VO_2. To determine L_{eff} in the M phase of $W_xV_{1-x}O_2$, we obtained κ_e^M in a similar way as for the undoped VO_2 nanobeams by considering both boundary scattering and the (now substantial) impurity scattering in the I and M phases of $W_xV_{1-x}O_2$.
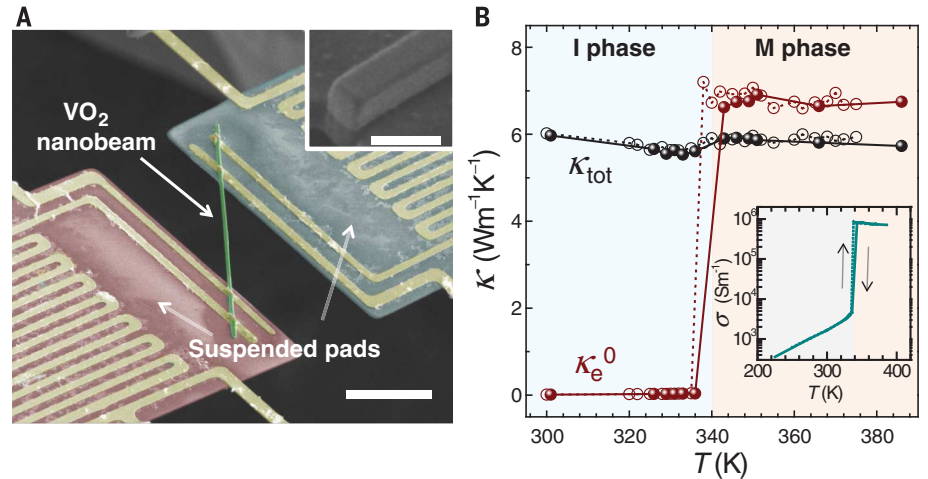
Fig. 1. Thermal conductivity of VO2 across the metal-insulator transition. (A) False-color scanning electron microscopy (SEM) image of a microdevice consisting of two suspended pads bridged by a VO_2 nanobeam. Thermal conductivity is measured by transporting heat from the Joule-heated pad (red) to the sensing pad (blue) through the nanobeam (green). (Inset) SEM image showing the rectangular cross section of a nanobeam. Scale bars: 10 μm (main panel); 500 nm (inset). **(B)** T dependence of measured total thermal conductivity (κ_{tot}) and expected electronic thermal conductivity ($\kappa_e^0 = L_0\sigma T$) of a VO_2 nanobeam. Filled (or open) symbols connected with solid (or dotted) lines are for data collected during heating (or cooling). κ_{tot} has a measurement uncertainty of < 5%, and T has an uncertainty of <0.7%. (Inset) Four-probe electrical conductivity (σ) versus T for the VO_2 nanobeam, used to calculate κ_e^0. Thermal and electrical contact resistances were found to be negligible.
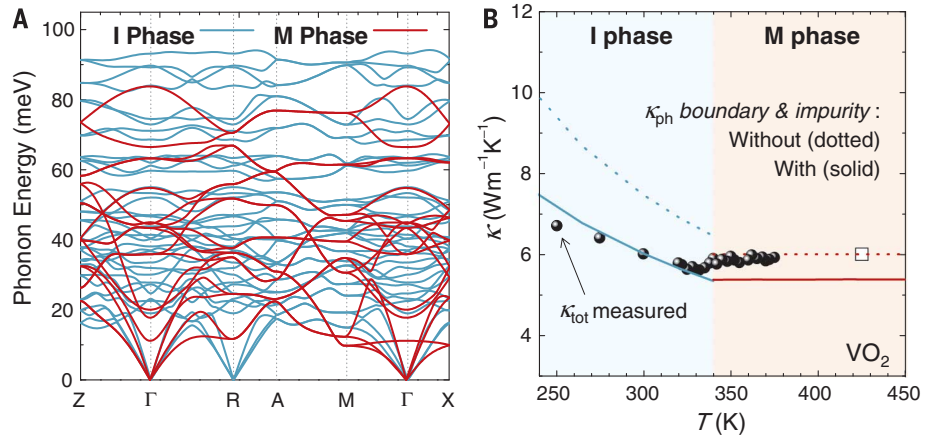

Fig. 2. Separating phonon thermal conductivity from electronic thermal conductivity. (A) I- and M-phase phonon dispersions from DFT calculations. To directly compare the phonon energy for the I and M phases, we plotted both dispersions together and used the rutile notation, with the zone boundary R point in the rutile M phase corresponding to the zone center Γ point in the monoclinic I phase. Z (0,0,0.5), R (0,0.5,0.5), A (0.5,0.5,0.5), M (0.5,0.5,0), X (0.5,0,0). **(B)** Nanobeam κ_{ph} (solid lines) in both I and M phases was calculated by combining κ_{ph}^{bulk} (dotted lines) with boundary and impurity scattering effects. The difference between the measured κ_{tot} and the nanobeam κ_{ph} gives κ_e^M. In the I phase, the DFT framework was used to calculate κ_{ph}^{bulk} according to the DFT-predicted phonon lifetimes; in the M phase, a similar framework was employed to calculate κ_{ph}^{bulk} using the phonon linewidths measured from IXS (25) on a bulk sample (open square). In the calculations, the IXS phonon linewidths for the M phase were considered independent of temperature, on the basis of the results reported in (25).

It can be seen from Fig. 3C that L_{eff} increases toward L_0 as a function of x (summarized in table S2).

In the $W_xV_{1-x}O_2$ samples, the average W-W distance is estimated to be ~1 nm, larger than our estimated quasiparticle mean free path of electrons in the M phase (~0.5 nm) (materials and methods section S10). With these levels of

W doping, the added elastic scattering from the dopants may partially contribute to the rise in L_{eff} for $W_xV_{1-x}O_2$. To elucidate the mechanism behind the vast suppression in L_{eff} and its partial recovery to the normal value with W doping, the Seebeck coefficient (S) of these nanobeams was also measured. The measured S can be used
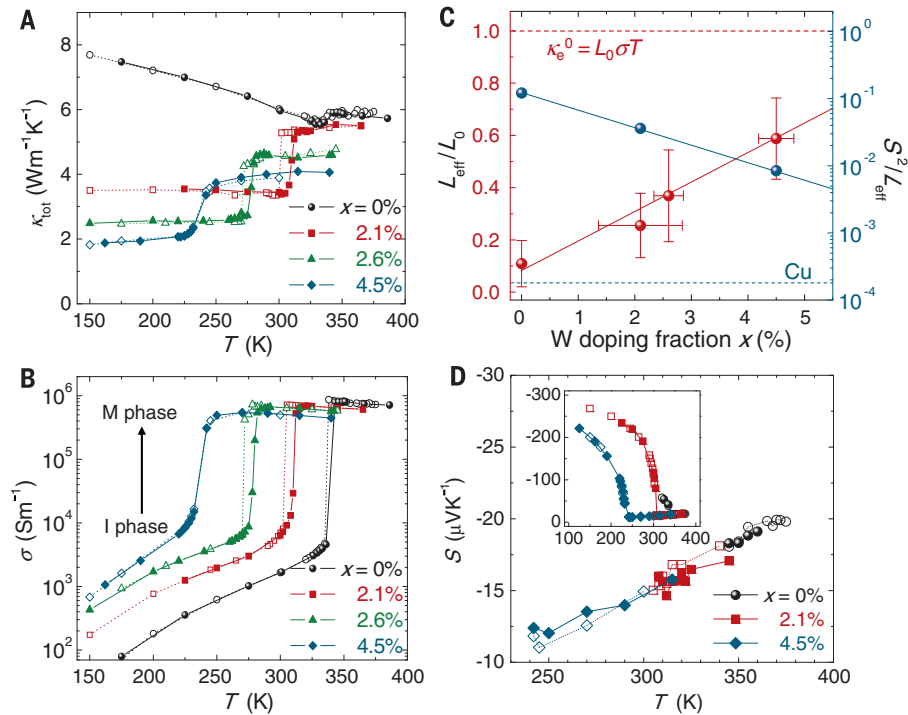
Fig. 3. Breakdown of the WF law from thermal and electrical conductivities of VO$_2$ and W$_x$V$_{1-x}$O$_2$ nanobeams. (**A**) Experimentally measured κ_{tot} of W$_x$V$_{1-x}$O$_2$ nanobeams. (**B**) Four-probe electrical conductivity σ versus T for the same set of W$_x$V$_{1-x}$O$_2$ nanobeams. T_{MIT} shifts toward lower T with W doping. (**C**) Extracted, normalized Lorenz number as a function of x. L_{eff} is obtained from $(\Delta\kappa_{tot} - \Delta\kappa_{ph})/(\sigma \cdot T)$, and the red solid line is a guide for the eye. Also shown is the M-phase S^2/L_{eff} with $x = 0$, 2.1, or 4.5% at T_{MIT} of 341, 312, and 240 K, respectively. The blue solid line is a guide for the eye. S^2/L_{eff} for a conventional metallic conductor, copper, is also shown for comparison (blue dashed line). Error bars mostly stem from uncertainties of total thermal conductivities and phonon linewidths. (**D**) Measured Seebeck coefficient S versus T for the M phase of the VO$_2$ and W$_x$V$_{1-x}$O$_2$ nanobeams. (Inset) S over a wider temperature range covering both the I and M phases. In all panels, filled (or open) symbols connected with solid (or dotted) lines represent the data collected during heating (or cooling).

to distinguish different scenarios that all lead to a very small L_{eff}. The dimensionless electronic figure of merit, $S^2/L = S^2\sigma T/\kappa_e$, is $\sim 10^{-4}$ for a conventional metal such as copper. Our measurements (Fig. 3C) instead show that $S^2/L_{eff} = 0.11$ for the M phase of VO$_2$ (summarized in table S2). Such a large value of S^2/L_{eff} for a metal is indicative of nonquasiparticle physics, because the factor k_BT/E_F (where E_F is the Fermi energy) that usually suppresses S is the same factor that suppresses interparticle interactions in a Fermi liquid. This is also supported by consideration of quasiparticle lifetimes (details in the supplementary materials). The quasiparticles, if present, would have a lifetime estimated to be on the order of $\hbar/k_BT$ (where $\hbar$ is Planck's constant h divided by 2π), described as the diffusive "Planckian" limit (28), characteristic of strongly interacting metals with T-linear resistivity (15). Independently and consistently, the M-phase VO$_2$ also exhibits a broad Drude peak with a width $> \sim k_BT$ in the optical conductivity (29, 30). Such a short lifetime cannot define meaningfully long-lived quasiparticles (14). Another closely related indication of the absence of quasiparticles in VO$_2$ is that its resistivity is above the Mott-Ioffe-Regel bound; hence, it is a "bad metal"

(31). A high value of S^2/L_{eff} approaching unity in strongly correlated, nonquasiparticle transport was also revealed in numerical studies using dynamical mean field theory (32, 33).

Without long-lived quasiparticles, transport of charge and heat must proceed through collective and independent diffusion (14). Hence, the Lorenz ratio of their conductivities has no reason to take the value L_0. Instead, the Lorenz ratio is proportional to the electronic specific heat over charge compressibility. For such systems in the high temperature limit (above the renormalized bandwidth), the temperature dependence of these thermodynamic quantities is relatively insensitive to interactions. Estimates then show that, in general, L_{eff} becomes very small, as the specific heat vanishes more rapidly than the charge compressibility with temperature (14) (see supplementary materials). Although L_{eff} numerically recovers toward L_0 with W doping, the linear temperature dependencies of the resistivity (Fig. 3B) and S (Fig. 3D) in the M phase are qualitatively unchanged. The collapse of S with different W doping levels onto the same temperature dependence, as well as the increase of resistivity with doping in the M phase, indicates that the material remains a "bad metal" with W doping,

suggesting the continued absence of long-lived quasiparticles. As T_{MIT} is lowered with doping, temperatures close to T_{MIT} (where L_{eff} is measured) are moving away from the asymptotic high-T regime. Therefore, at lower temperatures, although charge and heat diffusions remain independent, one no longer expects $L_{eff} \ll L_0$; instead, L_{eff} is expected to increase (14). A strong electron-phonon interaction may potentially couple κ_{ph} with κ_e, resulting in incomplete separability of κ_{ph} and κ_e in the M phase. However, the electron contribution to the observed κ_{tot} would still remain anomalously low, rendering VO$_2$ a model system to probe unusual charge behavior in "bad metals." As the decoupled, collective transport of charge and heat occurs universally in incoherent electron fluids, these effects are expected to exist generally in a wide variety of strongly correlated electron materials and can be explored with our experimental methodology. The Lorenz number thus provides a window into the unconventional electronic dynamics of these materials.

REFERENCES AND NOTES

1. C. L. Kane, M. P. A. Fisher, *Phys. Rev. Lett.* **76**, 3192–3195 (1996).
2. K. S. Kim, C. Pépin, *Phys. Rev. Lett.* **102**, 156404 (2009).
3. A. Garg, D. Rasch, E. Shimshoni, A. Rosch, *Phys. Rev. Lett.* **103**, 096402 (2009).
4. R. Mahajan, M. Barkeshli, S. A. Hartnoll, *Phys. Rev. B* **88**, 125107 (2013).
5. Y. Zhang et al., *Phys. Rev. Lett.* **84**, 2219–2222 (2000).
6. N. Doiron-Leyraud et al., *Phys. Rev. Lett.* **97**, 207001 (2006).
7. M. A. Tanatar, J. Paglione, C. Petrovic, L. Taillefer, *Science* **316**, 1320–1322 (2007).
8. H. Pfau et al., *Nature* **484**, 493–497 (2012).
9. Y. Machida et al., *Phys. Rev. Lett.* **110**, 236402 (2013).
10. J. K. Dong, Y. Tokiwa, S. L. Bud'ko, P. C. Canfield, P. Gegenwart, *Phys. Rev. Lett.* **110**, 176402 (2013).
11. R. W. Hill, C. Proust, L. Taillefer, P. Fournier, R. L. Greene, *Nature* **414**, 711–715 (2001).
12. J. Crossno et al., *Science* **351**, 1058–1061 (2016).
13. N. Wakeham et al., *Nat. Commun.* **2**, 396 (2011).
14. S. A. Hartnoll, *Nat. Phys.* **11**, 54–61 (2015).
15. J. A. N. Bruin, H. Sakai, R. S. Perry, A. P. Mackenzie, *Science* **339**, 804–807 (2013).
16. V. Eyert, *Ann. Phys. (Berlin)* **11**, 650–704 (2002).
17. C. N. Berglund, H. J. Guggenheim, *Phys. Rev.* **185**, 1022–1033 (1969).
18. V. N. Andreev, A. V. Chudnovskii, A. V. Petrov, E. I. Terukov, *Phys. Status Solidi, A Appl. Res.* **48**, K153–K156 (1978).
19. D. W. Oh, C. Ko, S. Ramanathan, D. G. Cahill, *Appl. Phys. Lett.* **96**, 151906 (2010).
20. B. S. Guiton, Q. Gu, A. L. Prieto, M. S. Gudiksen, H. Park, *J. Am. Chem. Soc.* **127**, 498–499 (2005).
21. Q. Gu, A. Falk, J. Wu, L. Ouyang, H. Park, *Nano Lett.* **7**, 363–366 (2007).
22. S. Lee et al., *J. Am. Chem. Soc.* **135**, 4850–4855 (2013).
23. P. Kim, L. Shi, A. Majumdar, P. L. McEuen, *Phys. Rev. Lett.* **87**, 215502 (2001).
24. S. Lee et al., *Nat. Commun.* **6**, 8573 (2015).
25. J. D. Budai et al., *Nature* **515**, 535–539 (2014).
26. A. K. McCurdy, H. J. Maris, C. Elbaum, *Phys. Rev. B* **2**, 4077–4083 (1970).
27. X. Tan et al., *Sci. Rep.* **2**, 466 (2012).
28. J. Zaanen, *Nature* **430**, 512–513 (2004).
29. M. M. Qazilbash et al., *Science* **318**, 1750–1753 (2007).
30. M. M. Qazilbash et al., *Phys. Rev. B* **74**, 205118 (2006).
31. V. J. Emery, S. A. Kivelson, *Phys. Rev. Lett.* **74**, 3253–3256 (1995).
32. J. Merino, R. H. McKenzie, *Phys. Rev. B* **61**, 7996–8008 (2000).
33. G. Pálsson, G. Kotliar, *Phys. Rev. Lett.* **80**, 4775–4778 (1998).

SUPPLEMENTARY MATERIALS

Editor's Summary

Decoupling charge and heat transport

In metals, electrons carry both charge and heat. As a consequence, electrical conductivity and the electronic contribution to the thermal conductivity are typically proportional to each other. Lee *et al.* found a large violation of this so-called Wiedemann-Franz law near the insulator-metal transition in VO$_2$ nanobeams. In the metallic phase, the electronic contribution to thermal conductivity was much smaller than what would be expected from the Wiedemann-Franz law. The results can be explained in terms of independent propagation of charge and heat in a strongly correlated system.

Science, this issue p. 371

Article Tools	Visit the online version of this article to access the personalization and article tools: http://science.sciencemag.org/content/355/6323/371
Permissions	Obtain information about reproducing this article: http://www.sciencemag.org/about/permissions.dtl

Supplementary Materials for

Anomalously low electronic thermal conductivity in metallic vanadium dioxide

Sangwook Lee,[†] Kedar Hippalgaonkar,[†] Fan Yang,[†] Jiawang Hong,[†] Changhyun Ko, Joonki Suh,

Kai Liu, Kevin Wang, Jeffrey J. Urban, Xiang Zhang, Chris Dames, Sean A. Hartnoll, Olivier

Delaire[*], Junqiao Wu[*]

† These authors contributed equally to this work.

* Corresponding authors. Email: wuj@berkeley.edu (J.W.); olivier.delaire@duke.edu (O.D.).

This file includes:

Materials and Methods

S1. Synthesis and characterization of VO_2 and $W_xV_{1-x}O_2$ nanobeams

The VO_2 and $W_xV_{1-x}O_2$ nanobeams were synthesized using a vapor transport scheme modified from a previously reported method (*20-22, 34*). Powder of V_2O_5 (and WO_2 if needed) was ground and well mixed, placed in a quartz boat at the center of a horizontal quartz tube furnace, and evaporated at 950°C (Fig. S1A). The ratio of the source powder, [W]/([W]+[V]), varied from 0 to 0.1 to control the tungsten doping fraction x in the final product. The evaporated V- and W-related species were transported by Ar carrier gas (6.8 sccm, 4 Torr). Downstream, free-standing nanobeams grew on an unpolished quartz substrate surface, as shown in Fig. S1B. All of the measured nanobeams have rectangular cross section, as confirmed by SEM imaging (inset of Fig. 1A). The lengths are typically tens of μm, and widths and thicknesses are in the range of a few hundred nm to a few μm. The phase of the nanobeams was verified by micro-Raman spectroscopy (Fig. S1C). Below their T_{MIT}, all nanobeams show the I phase with monoclinic $P2_1/c$ structure (also known as the M_1 structure) (*35*), which is the most stable phase of VO_2 below its T_{MIT}. There are no peaks related to other stoichiometries of vanadium oxides. All the Raman peaks disappear above their T_{MIT} (Fig. S1C), indicating the transition to the M phase with rutile $P4_2/mnm$ structure (also known as the R structure). The nanobeam axis is parallel to the c_R-axis (*c*-axis of rutile structure), confirmed by selected area electron diffraction (SAED), and consistent with previous reports (*21, 36*). The single-crystallinity of the nanobeams is confirmed by the fact that the SAED pattern remains identical when taken at different spots along the nanobeam length.
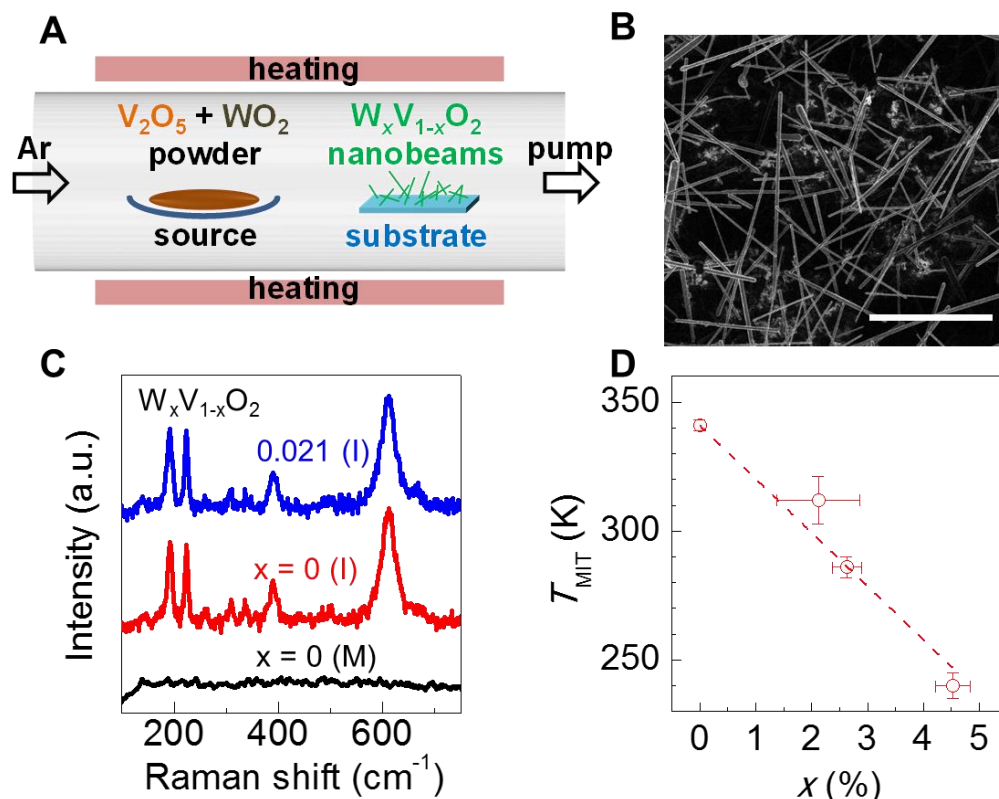
Fig. S1. (**A**) Schematic of growing the VO$_2$ and W$_x$V$_{1-x}$O$_2$ nanobeams. (**B**) A SEM image of as-grown W$_x$V$_{1-x}$O$_2$ nanobeams. Scale bar: 20 μm. (**C**) Raman spectra of an un-doped VO$_2$ ($x = 0$) and a W-doped VO$_2$ ($x = 0.021$) nanobeam recorded at room temperature. Both are identified as the I phase. Also shown is the M phase of the VO$_2$ beam measured at 360 K. (**D**) The MIT temperature as a function of AES-determined W doping fraction.

The W fraction (x) of W$_x$V$_{1-x}$O$_2$ nanobeams was evaluated using nano-Auger electron spectroscopy (AES) with a field emission electron source enabling ~ 10 nm probing spot size under ultra-high vacuum ($< 10^{-10}$ mbar). W bulk metal was used as the W reference material, and undoped VO$_2$ nanobeams were also measured for comparison. For each nanobeam, the Auger spectrum was measured ~ 10 times changing positions for an averaged spectrum. The W composition was determined employing the two tungsten MNN Auger peaks located at ~ 1730

3

eV and ~ 1793 eV. The W doping level is uniform along the nanobeam axis, verified by the nearly constant nano-AES signal along the nanobeam length. The T_{MIT} reduction rate by W doping was determined to be ~21K/at% (Fig. S1D), which is consistent with literature-reported values of ~20K/at% for single-crystal, W-doped VO_2 (*27*).

S2. Crystal structures of VO_2 in the I and M phases and the importance of using single-crystal nanobeams

All the measured nanobeams show the first-order phase transition from I (monoclinic M1, $P2_1/c$) phase to M (rutile R, $P4_2/mnm$) phase. Figure S2 shows the changes in V and O atomic positions across the phase transition. The phase transition was confirmed by a combination of optical imaging, electrical transport, and Raman spectroscopy. Across the MIT, nanobeams all show an abrupt jump in σ, by over ~ two orders of magnitude (Fig. 3B). Below the MIT temperature (T_{MIT}), σ increases exponentially with T as expected for a semiconductor. In the M phase above the T_{MIT}, all nanobeams exhibit metallic behavior, $i.e.$, σ decreasing slowly with T.
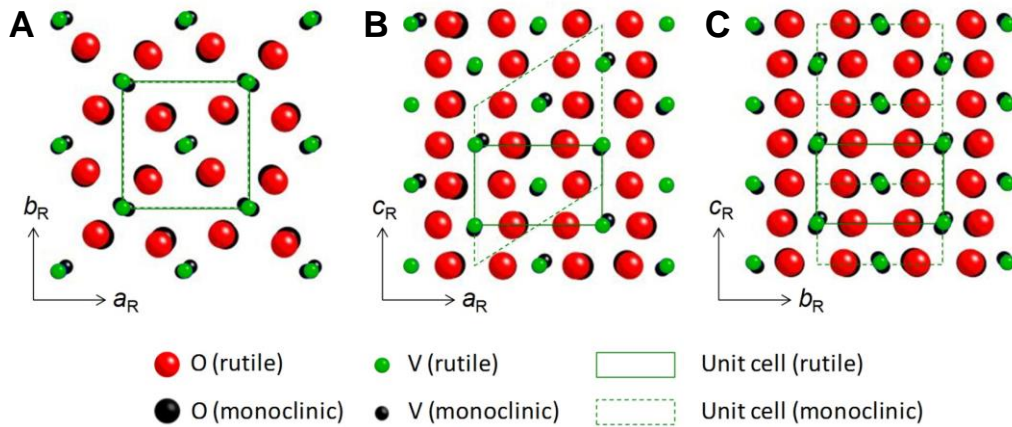
Fig. S2. Crystal structures of VO_2 projected along c_R-axis (**A**), b_R-axis (**B**), and a_R-axis (**C**). Monoclinic (I phase) and rutile (M phase) structures are superimposed onto each other to show the small lattice distortion across the phase transition.

It is known (*37-39*) that in large and/or polycrystalline VO_2 samples having a high density of crystal defects and/or clamping strain, the MIT typically progresses via gradual

evolution of microscopic M/I domain structures (*29*). As a result, intrinsic properties of the pure M and I phases could be obscured in transport measurements due to ensemble averaging over the M/I domains. In addition, the large (>1%) and anisotropic spontaneous strain associated with the MIT can also cause cracks and fatigue in these samples, which are responsible for degraded electronic and thermal properties. VO_2 nanobeams, on the other hand, can be made single-crystalline and free-standing (*37-39*). Free of extended structural defects and strain, these nanobeams undergo an abrupt, single-domain MIT, allowing unambiguous assessment of the intrinsic M- and I-phase properties. Most importantly, as stated in the main text, unlike in the case of thin film-based measurements, the nanobeam geometry ensures that both heat and charge flow in the *same* path along the nanobeam length direction. This is a crucial condition that, if unsatisfied, could result in erroneous determination of κ_e and assessment of the WF law, especially for VO_2 that has an anisotropic crystal structure.
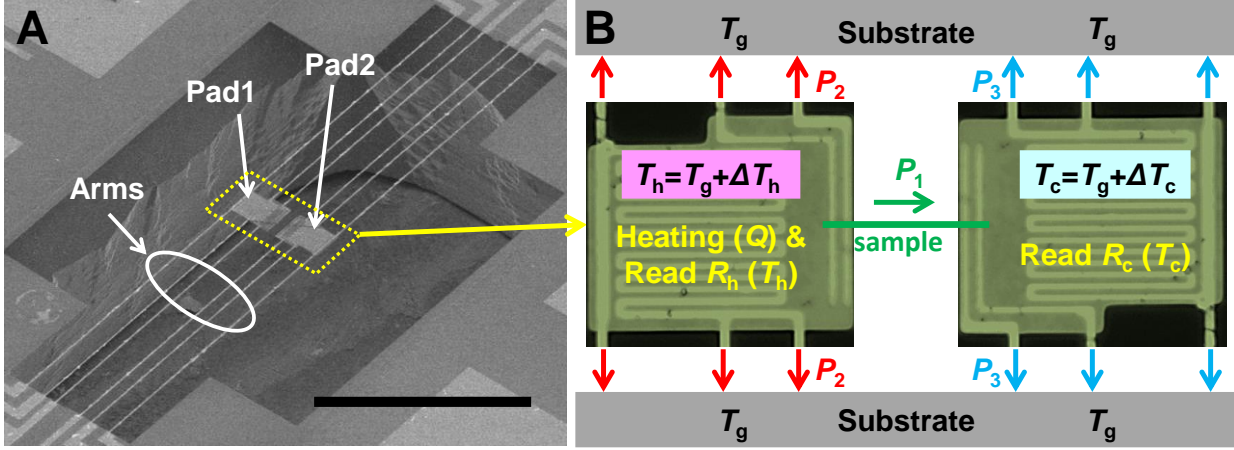
Fig. S3. Suspended-pad microdevice system. (**A**) SEM image showing two micro-pads, each suspended by six thin arms. Scale bar: 200 μm. (**B**) Schematic illustration of heat generation, transfer and dissipation in the suspended pad system. K_S of a nanobeam bridging the two suspended pads is measured by sensing T_h and T_c. Serpentine Pt electrodes connected to four arms are for sensing T_h and T_c. The four Pt electrodes crossed by the sample are for simultaneous four-probe electrical (σ) and Seebeck (S) measurements.

Suspended-pad microdevices (Fig. S3A) were used for the thermal conductance (K_S), electrical conductance (G) and Seebeck (S) measurements, similar to previous reports (*23, 24, 40*). Pt lines were patterned on SiN$_x$ pads each suspended with six flexural SiN$_x$ arms. The nanobeam is dry transferred to bridge the two suspended pads using a sharp probe tip by aid of a micromanipulator, and bonded onto the electrodes with Pt deposition using a focused ion beam (FIB) as electrical and thermal contacts. To secure the contacts, the devices were annealed at ~400 K for 1 h in a vacuum chamber before the measurements.

The straight Pt electrodes contacting the sample are used for the G measurements with the four-probe configuration. The serpentine Pt electrodes are used as micro-heater/thermometer, by applying DC current (I_h) to heat up and AC current to sense the temperature of each pad. Joule heat generated in the hot pad (Pad 1) will flow to the cool pad (Pad 2) through the nanobeam bridging the pads. The global temperature (T_g) is controlled by a cryogenic cooler and an extra heater that contacts the substrate through a sample holder. All the measurements were conducted inside a vacuum chamber ($<10^{-5}$ Torr).

K_S was measured as follows. Applying I_h on Pad 1 (Fig. S3B) generates the heat Q, raising the temperature of the Pad 1 to $T_h = T_g + \Delta T_h$. Some of Q will dissipate to the substrate (P_2) through the six arms of the Pad 1, and the rest will transfer to the Pad 2 (P_1) through the sample, raising the temperature of the Pad 2 to $T_c = T_g + \Delta T_c$. Finally, P_1 will dissipate to the substrate through the arms of Pad 2 (P_3). In the steady state, one can write the following equations:

$$Q = P_1 + P_2$$
$$P_1 = P_3$$
$$P_1 = K_s \times (T_h - T_c) = K_s \times (\Delta T_h - \Delta T_c) \quad , \qquad \text{(Eq.S1)}$$
$$P_2 = n \times K_{arm} \times (T_h - T_g) = n \times K_{arm} \times \Delta T_h$$
$$P_3 = n \times K_{arm} \times (T_c - T_g) = n \times K_{arm} \times \Delta T_c$$

where K_s and K_{arm} is the thermal conductance (K) of the sample and the arm, respectively, and n is the number of arms (*i.e.*, $n = 6$ in this work). Therefore,

$$K_s = (Q \times \Delta T_c) / (\Delta T_h^2 - \Delta T_c^2), \qquad \text{(Eq.S2)}$$

where Q is obtained by $Q = I_h^2 \times (R_{Pt} + R_{arm})$, and ΔT_h and ΔT_s can be measured by sensing the resistance of the serpentine Pt electrode on each pad. ΔT_h was controlled not to exceed 3K. 1.11 kHz (199 Hz) of AC current with a small amplitude < 500 nA was applied to measure the

resistance change of the serpentine Pt electrode on the Pad 1 (Pad 2). In order to calibrate the temperature of each pad, we used the resistance slope ($\Delta R/\Delta T$, where $\Delta T = 10$ K) at each global temperature as shown in Fig. S4 (100K in A and 300K in B). All the K_S in this study have < 5% measurement error. The total thermal conductivity κ_{tot} is obtained considering the geometric factor as $\kappa_{tot} = K_S \times l/A$, where A is the cross-sectional area, and l is the length of the nanobeam.
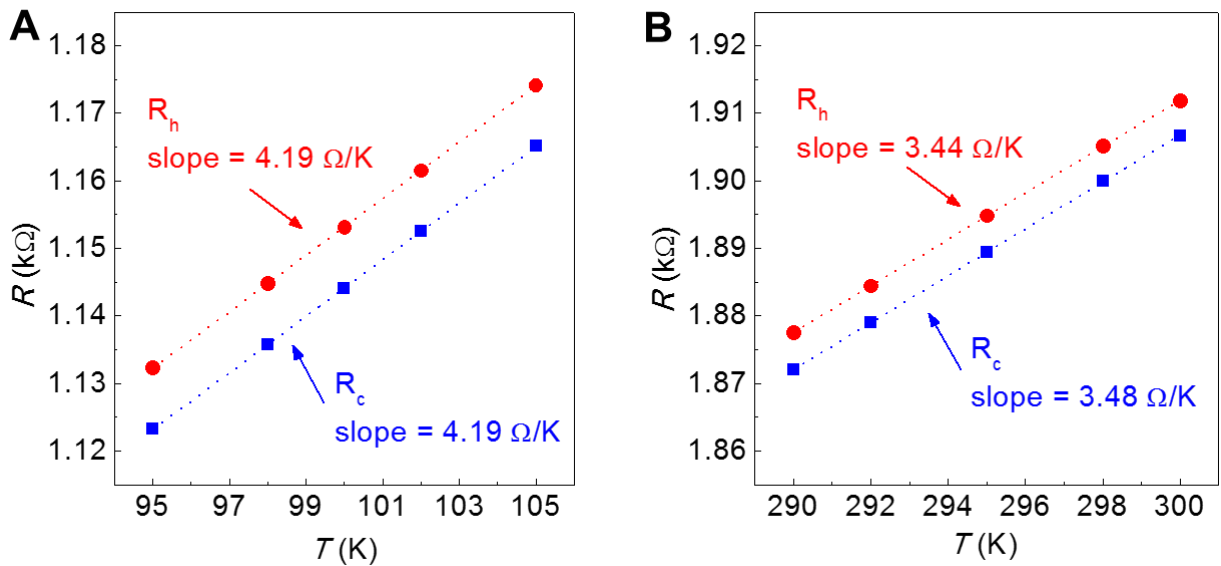
Fig. S4. R of serpentine Pt electrode vs. T of Pad 1 (R_h) and Pad 2 (R_c) on a microdevice. The fitted slopes are used to calibrate the ΔT_h and ΔT_s at the global temperature of (**A**), 100 K, and (**B**) 295 K. The coefficient of determination (R^2) of the fitted slopes is > 0.99996.

This system was calibrated by measurements of thermal conductivity of SiO_2 and crystalline silicon nanowires and compared against benchmark data (Fig. S5 below); the values of thermal conductivity were found to be similar to those reported in literature, such as Li *et al* (*41*) for Si and Cahill (*42*) for SiO_2 nanowires with similar diameters.
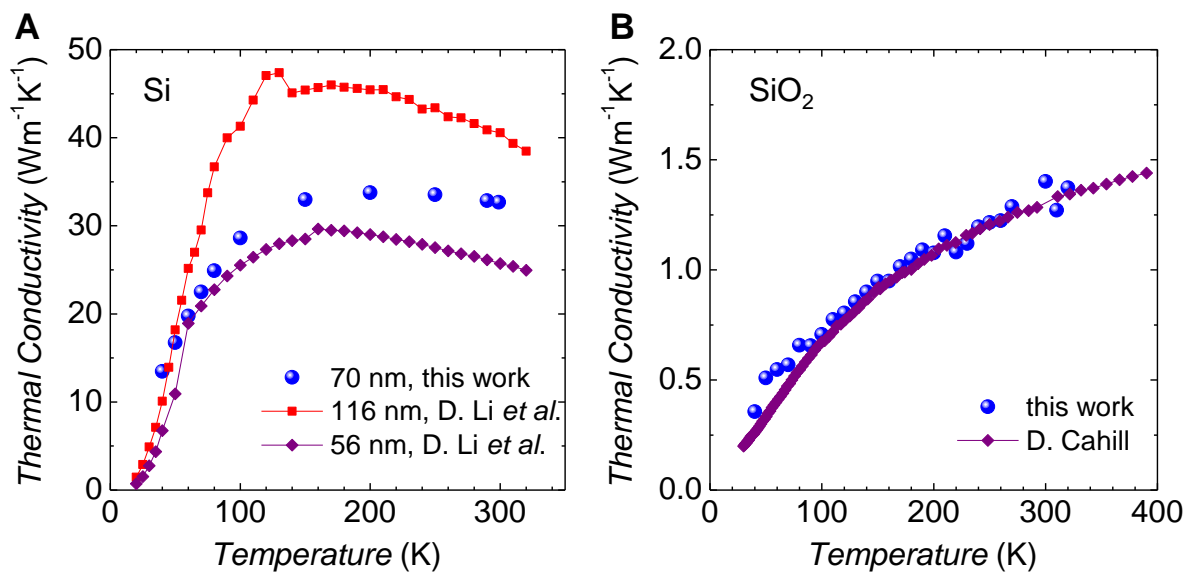
Fig. S5. This system was calibrated by measurements of thermal conductivity of silicon and SiO₂

nanowires and compared against benchmark data, and good agreements were found.

S4. Negligible strain effects and electrical and thermal contact resistances

Unlike ordinary devices used for electrical transport measurements where the samples are firmly clamped on a solid substrate, in our case the two pads suspended by the long, flexural arms are free to move toward or away from each other, thus the nanobeam is free to shrink or elongate and the development of axial strain is avoided (*22*). This is important, because if it is not satisfied, multiple M/I domains will develop along the nanobeam, which would complicate the electrical/thermal conduction (*36, 38*), and the M/I junctions would also contribute to additional Seebeck voltages (*43*).

The Pt bonds make good Ohmic electrical contacts between the electrodes and the nanobeams, as evidenced by the linear I-V curves and the agreement between two- and four-probe measured electrical resistances of nanobeams (Fig. S6A). The I-V curves are linear in both the I and M phases (Fig. S6B). The measured electrical conductivity (σ) of undoped VO_2 is within a reasonable range of values reported in the literature for single-crystal VO_2, as compared below in Table S1. This level of difference in σ can arise from the sample quality (more sample quality discussion in Supplementary Materials S6).

References	Our work	Ladd *et al.* (*44*)	Burglund *et al.(17*)	Allen *et al.(45*)	Nakano *et al.* (*46*)
σ (S/m)	~ 8×10^5	~ 10×10^5	~ 5×10^5	~ 5×10^5	2×10^5
Specimen crystallinity	Single crystal	Single crystal	Single crystal	Single crystal	Thin film (10-70 nm)

Table S1. Experimental electrical conductivity of VO_2, and comparison to literature values.

The thermal contact resistance between the nanobeam and the suspended pads in both the I and M phases was also found to be negligible, as verified by length-dependent measurements in

Fig. S6C. The thermal contact resistance is obtained by extrapolating this dependence to zero as in the following:

$$R_{tot} = R_{ct} + R_s = R_{ct} + L_s/\kappa_s A_s, \qquad\qquad (Eq.S3)$$

where R_{tot} is the total thermal resistance [K/W], R_{ct} the total thermal resistance of the contacts [K/W], R_s the thermal resistance of the sample [K/W], κ_s the thermal conductivity of the sample [W/m·K], A_s the sample cross sectional area [m^2], L_s the sample length, and A_{ct} the contact area [m^2]. Importantly, because the intercept R_{ct} in Fig. S6C is much smaller than R_s, the thermal resistance R_{ct} of all the contacts is negligible, which is consistent with conclusions in literature using similar method to make contacts, such as Pt/VO$_2$ contact (47) and Pb/C-bond contact (48).

To analyze further, the contacts' contribution R_{ct} (2.2 - 4.3 ×10^5 K/W) amounts to only 0.6 ~ 3.9% of the nanobeam's total resistance R_{tot} (1.1 - 3.7 ×10^7 K/W) with the length shown in Fig. S6C. With the typical area A_{ct} of 5.6 × 10^{-13} m^2 (contact area for the undoped VO$_2$ sample), we evaluate the thermal contact resistance per unit area ($R^{"}_{ct} = A_{ct}R_{ct}$) to be $R^{"}_{ct}$ = 1.2 - 2.4 × 10^{-7} m^2·K/W. This level of $R^{"}_{ct}$ is within an order of magnitude to that of ultra-high quality, atomically-intimate contacts realized by sputtering and evaporation (19, 49).
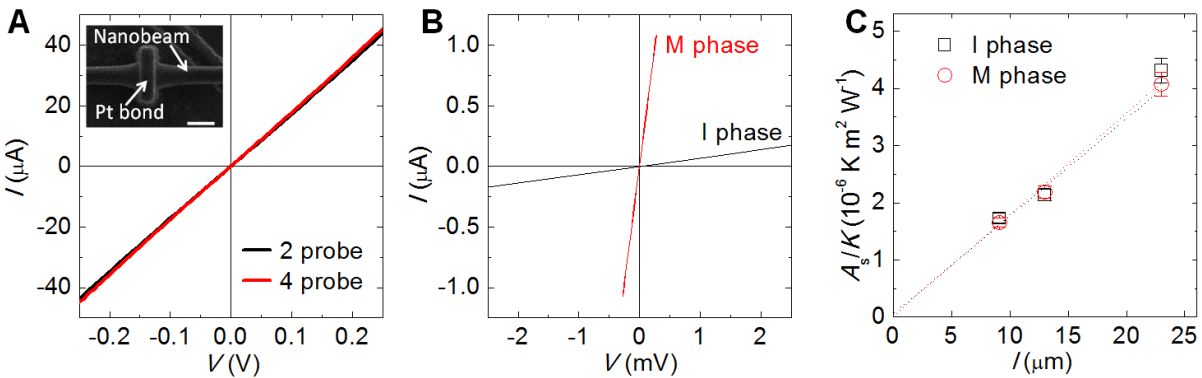
Fig. S6. (**A**) I-V curves of an undoped VO$_2$ nanobeam (I-phase) measured in the two-probe and four-probe configuration, where the electrodes were made with FIB Pt bonding. The nearly

identical I-V curves show that the electrical contact resistance is negligible. Inset shows SEM image of a Pt-bonded contact between the nanobeam and the underlying pad electrode. Scale bar: 500 nm. (**B**) Linear I-V curves of an undoped VO_2 nanobeam in the I and M phases. (**C**) Plot of total thermal resistance $(1/K)$ multiplied by cross-sectional area (A_s) of the nanobeams (each beam has a different A_s) as a function of the nanobeam length (l). Here the nanobeams are undoped VO_2. The linear relationship and the fact that they extrapolate to zero indicate negligible thermal contact resistance.

S5. Determination of nanobeams sizes
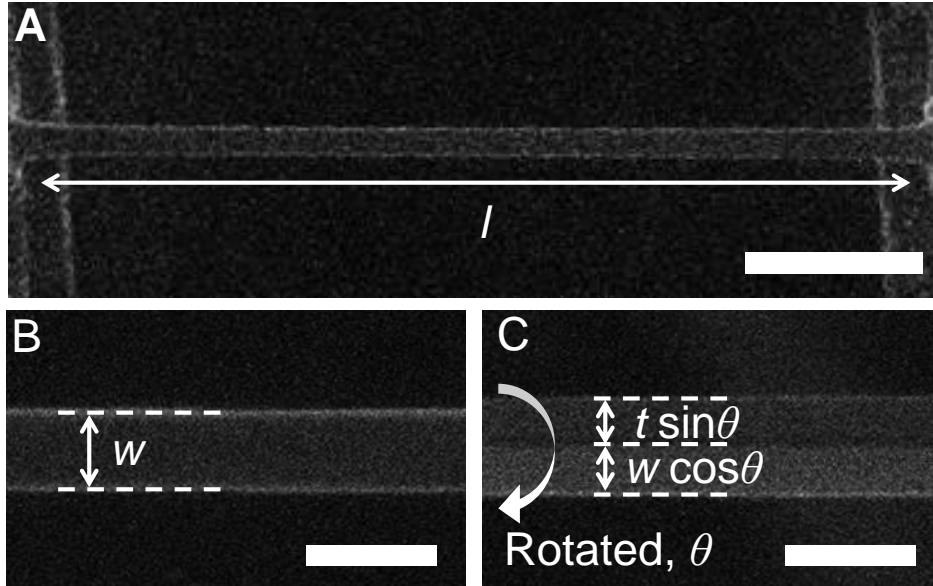
Fig. S7. SEM images of a typical nanobeam on the device, taken in the top view (**A-B**), and at a tilted angle (**C**). Scale bar: (**A**) 2 μm; (**B**) 500 nm; (**C**) 500 nm.

To accurately determine κ and σ of the nanobeams, it is important to carefully measure the nanobeam dimensions. The length (l) and width (w) of the nanobeams were measured using a SEM. To measure the thickness (t), the image was taken at a tilted angle by rotating along the axis of the nanobeam, as shown in Fig. S7. All the dimensions were measured using a SEM with the resolution of ~5 nm/pixel. As the thinnest nanobeams have $t > 200$ nm, a maximum error of 4.3% could occur in the geometric factor ($A/l = t \times w/l$). However, even in this case, the size error does not affect the evaluation of $\Delta\kappa_e/\kappa_{tot}$. The error from the size measurements does not translate to the effective Lorenz number L_{eff}, because the geometric factor is cancelled out in calculating L_{eff}.

S6. Effects of vacancies and twin boundaries, and more devices measured

The MIT temperature is dependent on the stoichiometry of VO_2: a small change in the oxygen concentration results in a shift in T_{MIT} (*50*). Since all of our VO_2 nanobeams have a MIT at the un-shifted 340K, we expect the non-stoichiometry deviation from $VO_{2.0}$ to be less than 1%. In addition, oxygen vacancies affect the electrical conductivity in the I phase (*51*), but its contribution to electronic thermal conductivity is negligible, as the electrical conductivity is always very low in the I phase compared to the M phase. Twinning in the I phase may occur during growth or due to clamping strain in thin films or nanobeams supported on a substrate (*52, 53*). Our nanobeams are suspended with the flexural platforms and hence strain-free (*22*). Nonetheless, it is possible that a small number (< 10) of twin walls form during the growth distributed at random positions along the nanobeam length in the I phase (*52*). However, the distance between the twin walls is expected to be much larger than the effective diameter of the nanobeams, and hence their effects on thermal conductivity of the I phase are minimal. Moreover, when undergoing the MIT into the M phase for which the Lorenz number is analyzed in this work, these twins disappear, because they are forbidden by the tetragonal crystal symmetry (*52*).

Indeed, these effects on thermal conductivity are negligible, as seen from reproducibility of the measured results: multiple nanobeams synthesized in different growth batches demonstrate reproducibly very similar value and behavior of κ_{tot}, despite their possible different twin structures. As shown in Fig. S8, we have measured more VO_2 nanobeam devices, and all devices show consistently anomalously small change in κ_{tot} across the MIT.
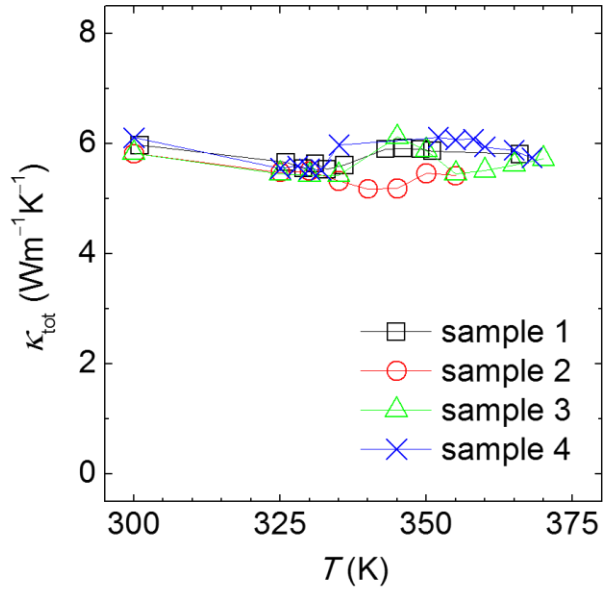
Fig. S8. Measured κ_{tot} of four undoped VO_2 nanobeams, all showing very similar behavior as the one in Fig.1B: nearly no change or changes across the MIT much lower than κ_e^o expected from the WF law using L_0.

S7. Bulk phonon thermal conductivity

To analyze the anomalously small change $\Delta\kappa_{tot}$ across the MIT in undoped VO$_2$, the

naïve assumption that the phonon contribution to κ_{tot} in the I and M phases are equal ($\kappa_{ph}^{I} = \kappa_{ph}^{M}$)

can be first considered. The measured $\Delta\kappa_{tot}$ can then originate only from the change in κ_e, that is,

$\Delta\kappa_{tot} = \Delta\kappa_e = \kappa_e^{M}$, since κ_e^{I} in the I phase is negligible. We define the effective Lorenz number

in the M phase, L_{eff}, following the formulation of the WF law, $\kappa_e^{M} = L_{eff}\sigma T$, such that

$L_{eff}/L_0 = \kappa_e^{M}/\kappa_e^{0}$. This analysis is similar to that by Núñez-Regueiro $et\ al$ on TaS$_2$ across its

charge-density-wave transition (54), and by Crossno $et\ al$ in hydrodynamic electron behavior in

graphene (12). Under this assumption, L_{eff}/L_0 of VO$_2$ would clearly be extraordinarily low: about

0.04.

For W$_x$V$_{1-x}$O$_2$ nanobeams, although $\Delta\kappa_{tot}$ is much higher than in the undoped VO$_2$

samples, the analysis based on the WF law using L_0 would still lead to a similarly unrealistic

conclusion. For example, for the W$_{0.021}$V$_{0.979}$O$_2$ nanobeam, κ_e^{0} is estimated to be 5.3 W/m·K in

the M phase based on the measured σ, which is nearly equal to $\kappa_{tot}^{M} = 5.4$ W/m·K; hence a direct

application of the WF law using L_0 would require unrealistically that $\kappa_{ph}^{M} = \kappa_{tot}^{M} - \kappa_e^{M} \approx 0$.

Therefore, for both the undoped and W-doped VO$_2$, the actual value of κ_{ph} and the

change in κ_{ph} across the transition both must be considered carefully.

In general, κ_{ph} is determined by the product of the mode-dependent lattice specific heat

($C_{q,j}$), phonon group velocity ($v_{q,j}$), and the mean free path ($\Lambda_{q,j} = v_{q,j}\,\tau_{q,j}$, where $\tau_{q,j}$ is the phonon

scattering time, q the phonon mode wavevector, and j the phonon branch index), which are

dominated by the harmonic (C, v) and anharmonic (τ) parts of the interatomic potentials. The

monoclinic structure (P2₁/c) of the I phase differs from the tetragonal structure (P4₂/mnm) of the M phase only by a small lattice distortion, as shown in section S2. The total lattice specific heat ($C = \Sigma_{q,j}C_{q,j}$) is related to the total number of phonon modes and is not very different between the I and M phases, as confirmed by measurements (*17*). The sound velocity $v \sim (Y/\rho)^{1/2}$ is expected to be slightly different, as both the Young's modulus (*Y*) (*55*) and density (ρ) of VO_2 show small variation between these two phases. Indeed, the measured Rayleigh sound velocity of surface acoustic waves in VO_2 along the c_R-axis was reported to change by ~ 10% between the I and M phases (*56*). Furthermore, inelastic neutron scattering measurements (INS) showed that the phonons are softer in the metallic phase than in the insulating state (*25*). The softening of phonon group velocities across the MIT is more directly revealed in the first-principles simulations of phonon dispersions for both phases (Fig. 2A). Lastly, τ is expected to change across the MIT, predominantly due to higher phonon anharmonicity in the M phase (*25*). For example, the thermal expansion coefficient, which reflects the anharmonicity, is higher in the M phase than the I phase by a factor of two (*57*). Therefore, it is anticipated that $\kappa_{ph}^M < \kappa_{ph}^I$ in the bulk, and hence κ_{ph} must be considered carefully, to understand the unusually small change in the measured κ_{tot}.

A. DFT calculations of dispersions for both I and M phases of VO_2:

The κ_{ph} of the undoped VO_2 was calculated based on the first-principles calculations performed in the framework of DFT as implemented in the Vienna *ab initio* Simulation Package (VASP)(*58, 59*) with a plane-wave cut-off of 500 eV. An 8× 8×8 Γ-centered *q*-point mesh is used for the M and I phases. The projector augmented-wave potentials explicitly include 13 valence electrons for V ($3s^23p^64s^2\,3d^3$) and 6 for oxygen ($2s^22p^4$). The PBE exchange-correlation functionals (*60*) were used in the calculations. The supercell was chosen as 2×2×5 for the M

phase (5 unit cells along c) and $2\times2\times2$ for the I phase. The harmonic phonon dispersion calculations were performed with VASP and Phonopy (*61*).

The monoclinic I phase was found to be harmonic and phonon dispersions were computed as described above. We note that harmonic DFT dispersions reported here for the monoclinic I phase are in excellent agreement with the phonon dispersions measured on bulk single crystals with inelastic x-ray scattering (IXS). The rutile M phase was found to be highly anharmonic in our DFT calculations, also consistent with the recently reported IXS measurements in Ref. (*25*). For the rutile M phase of VO_2, DFT calculations limited to the harmonic approximation yield unstable phonon branches over much of the Brillouin zone, independent of the exchange-correlation functional and other parameters of the simulation. IXS measurements revealed very broad acoustic modes, confirming the strong anharmonicity. In order to capture the anharmonic renormalization of phonons in the rutile M phase, first-principles calculations at finite temperature (425K) were performed with *ab initio* molecular dynamics (AIMD) in the canonical ensemble (NVT), and the temperature-dependent effective potential (TDEP) method (*62*) for a $2\times2\times5$ supercell of rutile (M-phase) unit cell. This procedure yielded renormalized dispersions in good agreement with IXS data reported in Ref.(*25*).

B. Phonon thermal conductivity calculations for the bulk I and M phases:

The intrinsic (bulk) thermal conductivity of the respective VO_2 phase was obtained by integration over the Brillouin zone for the different branches:

$$\kappa_{\alpha\beta} = \frac{1}{V}\sum_{\lambda} C_{\lambda} v_{\alpha\lambda} v_{\beta\lambda} \tau_{\lambda}, \qquad\qquad (\text{Eq.S4})$$

where $\lambda = (\boldsymbol{q}, j)$ labels each phonon mode (wave vector, branch index). The mode contribution to the volumetric heat capacity is

$$C_\lambda = \hbar \omega_\lambda \frac{\partial n_\lambda^0}{\partial T} = \frac{\left(\hbar \omega_\lambda\right)^2}{k_B T^2} n_\lambda^0 \left(n_\lambda^0 + 1\right). \tag{Eq.S5}$$

And the mode-dependent group velocity is evaluated from the derivative of the dynamical

matrix,

$$v_{\alpha\lambda} = \frac{\partial \omega_\lambda}{\partial q_\alpha}. \tag{Eq.S6}$$

The Bose distribution was computed for the respective temperature T,

$$n_\lambda^0 = \frac{1}{e^{\hbar \omega_\lambda / k_B T} - 1}. \tag{Eq.S7}$$

For the monoclinic I phase, we calculated the phonon thermal conductivity fully from first-

principles, using the Boltzmann transport equation (BTE) formalism implemented in the

software ShengBTE (*63*).

The calculated thermal conductivity for bulk, monoclinic I phase of VO$_2$ at $T = 340$K is

$\kappa_{ph}^{I,bulk} = 6.46$ W/m·K.

For the rutile M phase, we used the dispersions and group velocities obtained from DFT

(via TDEP) shown in Fig.2A at 425 K. The phonon lifetimes τ_λ in the rutile phase were based on

the experimentally measured data reported in Ref.(*25*), which shows no temperature dependence

up to 425K as long as VO$_2$ is in the M phase. In order to carry out the integration for $\kappa_{\alpha\beta}$ in Eq.

S4 over the Brillouin zone, we obtained an empirical relationship between the set of reported τ_λ

and the phonon energies. A simple correlation was obtained for the phonon scattering rates,

$1/\tau_{q,j}$, versus phonon energy. For the phonon modes measured over the dispersive portion of the

acoustic branches (TA modes: $E < 12$meV, LA modes $E < 30$meV), we found a linear correlation

(*i.e.*, $h/\tau_{q,j} \approx \alpha E_{q,j}$, where $\alpha = 0.21 \pm 0.02$ and h is the Planck constant), as shown in Fig. S9. As

was noted in Ref.(*25*), the TA phonon modes are especially broad for the flat portions of the dispersions, *e.g.*, around the R and M symmetry points of the rutile Brillouin zone. However, since these modes have very low group velocities, they do not contribute significantly to the thermal conductivity, and details of the scattering rates are less important. In consequence, we simplify the correlations between $1/\tau_{q,j}$ and E to be the same for all modes.

The thermal conductivity integration was performed by summing Eq.S4 over the symmetry-irreducible wedge of a 20×20×20 reciprocal space q-grid, including all the branches. The group velocities were evaluated numerically from the dispersions surfaces calculated on the q-grid. The convergence with grid density was checked.

The result for the bulk rutile M phase of VO₂ at $T = 425$K is $\kappa_{ph}^{M,bulk} = 5.72$ W/m·K.
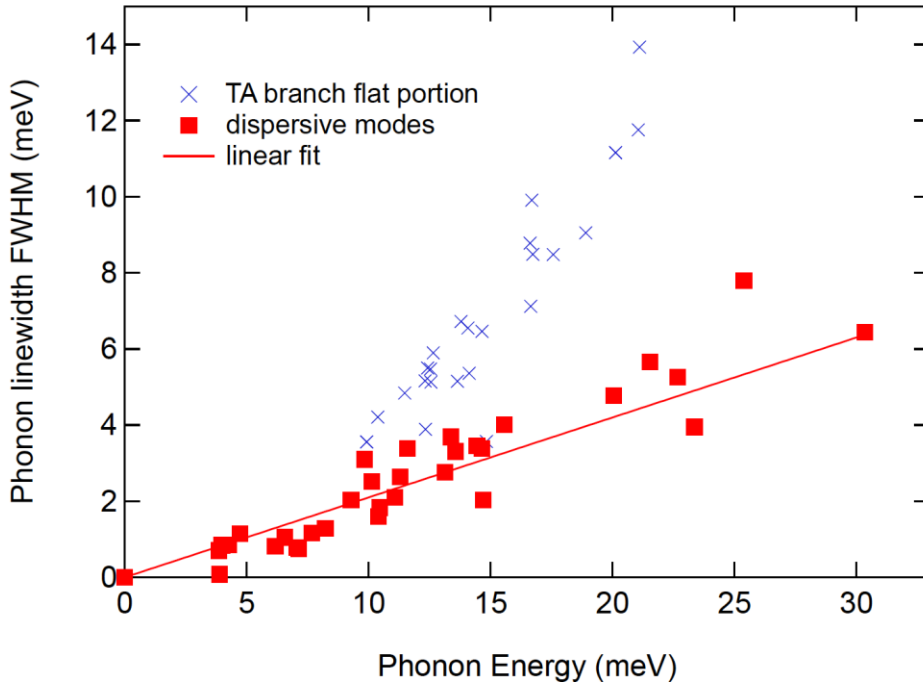

Fig. S9. Full-Width-Half-Maximum (FWHM) for dispersive (filled squares) and non-dispersive (crosses) phonon modes in the M phase at 425K, extracted from the Inelastic X-Ray Scattering (IXS) measurements on bulk VO₂ reported in Ref. (*25*), which is subsequently used to extract the

phonon thermal conductivity of the M phase using $h/\tau_{q,j}$ = FWHM. Data at 342K shows the same dependence.

We also calculated mode-resolved phonon MFPs in each phase as shown in Fig. S10. The MFPs for the metallic phase were obtained from the first-principles group velocities and IXS measurements of phonon linewidths (see also Fig. S9), while the MFPs for the insulating phase were obtained from group velocities and linewidths both computed from first-principles. Focusing on modes below 25 meV, which are the dominant heat carriers around room temperature, the average phonon MFP is 5.18 nm for the metallic phase and 5.86 nm for the insulating phase, respectively, which are very similar to each other. Figure S10 shows that some of the low-energy phonons (below 10 meV) have much larger MFPs in the insulating phase than the metallic phase, but the insulating phase also exhibits numerous phonon modes with very small MFPs, which is a result of its many optical branches with very low group velocities (as seen in Fig. 2A). As a result, the average phonon MFPs are fairly similar for both phases. Therefore, the lattice thermal conductivities of both phases are similar across the MIT.
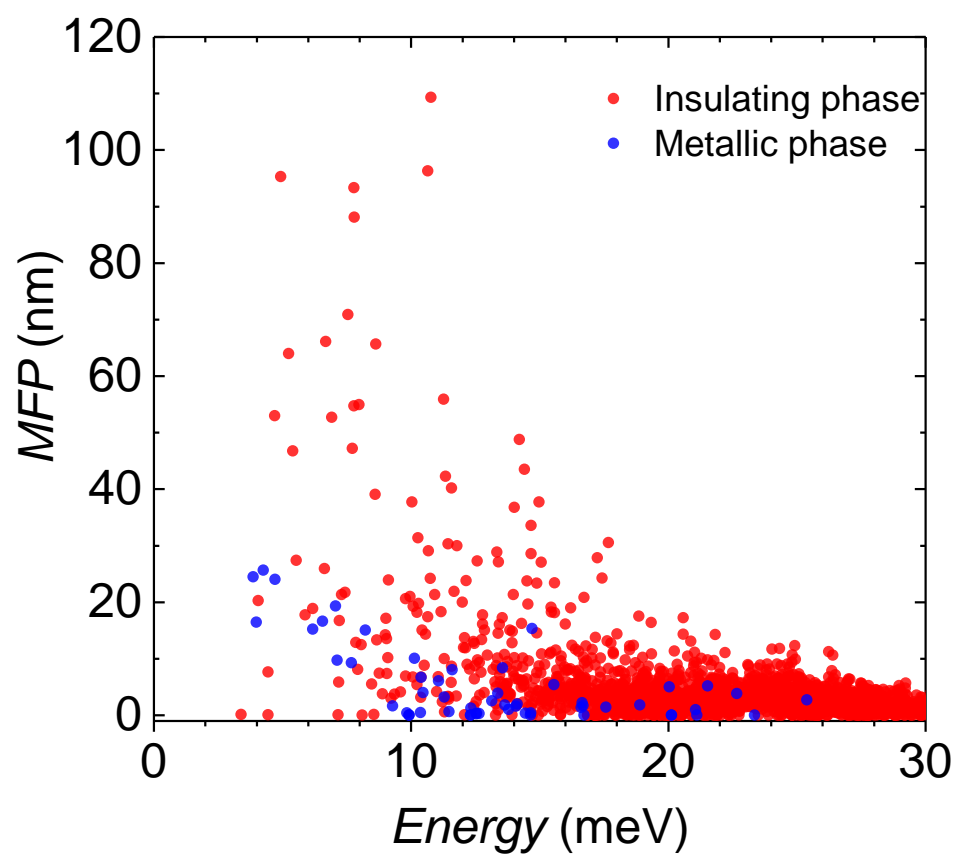
Fig. S10. Mode dependent phonon mean free paths (MFPs) of VO$_2$ in the insulating phase at 340 K and metallic phase at 425 K.

S8. Nanobeam phonon thermal conductivity

We obtain the nanobeam thermal conductivity by using Matthiessen's rule to combine different scattering mechanisms in the nanobeams. We start from I phase bulk thermal conductivity $\kappa_{ph}^{I,bulk}$ (= 6.46 W/m·K from DFT in Section S7) of undoped VO_2 at the phase transition temperature of 340K, where the dominant scattering mechanism is umklapp scattering. With this $\kappa_{ph}^{I,bulk}$, adding boundary scattering using Eq.14 in Ref. (*26*) (as the effective beam size shown in Table S2) and impurity scattering using the Klemens' expression (*64*) of $\tau_{impurity,I}^{-1} = A_I\omega^4$, the nanobeam phonon thermal conductivity can be obtained. Fitting to our measured I-phase nanobeam thermal conductivities (Fig. 3A of the main text) in the temperature regime near the MIT, the only unknown parameter A_I can be obtained. For the samples with 2.1%, 2.6%, and 4.5% W-doping, the A_I values are 2.8×10^{-42} s^3, 7.8×10^{-42} s^3 and 1.5×10^{-41} s^3, respectively. We note that effects of any local strain (bond deformation) due to the W doping are also effectively included together with the impurity scattering in this model. The undoped VO_2 may also have impurity scattering due to native defects. The corresponding A_I value from fitting is 2.3×10^{-43} s^3, orders of magnitude smaller than the $W_xV_{1-x}O_2$. In the undoped VO_2 nanobeams, the thermal resistance contributed by the impurity scattering is one order of magnitude lower than the resistance limited by umklapp scattering. Thus, the uncertainty in A_I would not affect the main conclusions of unusually low electronic thermal conductivity (κ_e^M) and low effective Lorenz number ($L_{eff} << L_0$) in the undoped nanobeams.

For the impurity scattering in the M phase, while the species and density of impurities remain unchanged across the MIT for any given sample, the scattering cross-section is scaled by the phonon group velocity, and we accounted for this effect by using the respective dispersions

of I and M phases along the c_R axis. Based on the impurity scattering time in I phase, we obtained the impurity scattering time in M phase of all the acoustic branches using Klemens' expression (*64*) of $\tau^{-1}_{\mathrm{impurity,M}} = A_M \omega^4$, where $A_M = \left(v_M / v_I\right)^3 A_I$, and v_I and v_M are the group velocities of the I and M phase for their corresponding branches along the c_R axis. These group velocities were extracted from the calculated dispersion in Fig. 2A. The boundary terms are the same in the M and the I phases. All the other scattering mechanisms in the M phase were included in the experimental linewidths determined from the IXS measurements of the bulk single crystal (*25*). With these individual components ascertained, the phonon thermal conductivity of the M phase of VO_2 and $W_x V_{1-x} O_2$ nanobeams was obtained. Subtracting this phonon contribution κ^M_{ph} from the measured κ^M_{tot}, κ^M_e was obtained, as seen in Table S2. For the undoped VO_2, the obtained κ^M_e (0.72 W/m-K) is small compared to the measured κ^M_{tot} (5.87 W/m·K). Although the uncertainty for κ^M_e is large compared to κ^M_e itself (~80% for VO_2), this does not affect the fact that L_{eff}/L_0 is still small: the upper bound of L_{eff}/L_0 for VO_2 is less than 0.2 even when considering such uncertainty, as shown by the error bars in Fig. 3C.

W doping fraction, x (%)	MIT temperature (K)	Effective beam size (nm)	κ^I_{tot} (W/m·K)	κ^M_{tot} (W/m·K)	κ^M_{ph} (W/m·K)	κ^M_e (W/m·K)	L_{eff}/L_0 at T slightly above T_{MIT}
0	341	432	5.80	5.87	5.15	0.72	0.11
2.1	312	325	3.4	5.32	3.98	1.34	0.26
2.6	286	512	2.63	4.46	2.83	1.63	0.37
4.5	240	508	1.99	3.96	2.19	1.77	0.59

Table S2. W-doping dependent metal-insulator phase transition temperature T_{MIT}, effective beam size, and normalized Lorenz number at temperatures slightly above T_{MIT}. Thermal conductivity of the phonon contribution, electron contribution, and the total are also shown for both the M and I phases.

S9. Seebeck coefficients of VO$_2$ and W$_x$V$_{1-x}$O$_2$ nanobeams

Seebeck coefficients (S) were measured using the suspended-pad microdevices. When we measured the electric potential (V_{total}) produced by a temperature difference $\Delta T = T_h - T_c$, the measured S ($S_{measured}$) includes the potential drop across the two platinum arms that support the hot pad ($V_{Pt,h}$) and cool pad ($V_{Pt,c}$), as follows:

$$S_{measured} = -\frac{V_{total}}{T_h - T_c} = -\frac{V_{total}}{\Delta T} \qquad \text{(Eq.S8)}$$

$$V_{total} = V_{Pt,h} + V_{NB} + V_{Pt,c} \qquad \text{(Eq.S9)}$$

where V_{NB} is the potential produced across the nanobeam sample. $V_{Pt,h}$ and $V_{Pt,s}$ are generated by the temperature difference between the hot pad and substrate [$V_{Pt,h} = -S_{Pt}(T_0 - T_h)$], and the cool pad and substrate [$V_{Pt,c} = -S_{Pt}(T_c - T_0)$], respectively, hence one obtains the following:

$$S_{measured} = -\frac{V_{total}}{\Delta T} = -\frac{-S_{Pt}(T_c - T_h) + V_{NB}}{\Delta T} = -S_{Pt} + S_{NB} \qquad \text{(Eq.S10)}$$

The S_{NB} shown in Fig. 3D was obtained using the $S_{measured}$ and previously reported S_{Pt} (65). It is intriguing to note that the Seebeck coefficients of the metallic phase of VO$_2$ measured from different samples and reported by different groups (17, 43, 66) are all very close to each other, between 20-30 µV/K, despite that the S values for the insulating phase are vastly different.

The measured Seebeck coefficient for these different samples collapses into the same temperature dependence, as shown in Fig. 3D. This is consistent with the continued absence of quasiparticles even after the W doping. For VO$_2$, its Seebeck coefficient is one order of magnitude higher than most good metals, which are defined as metals where the electron mean free path (l_e) is well defined and is much larger than the Mott-Ioffe-Regel limit, $l_e > a$, where a is the lattice spacing (67). Further, even at lower temperatures, the slope of S versus T is

significantly larger (~ 6 µV K^{-1}/100K) than those for good metals (~ 0.5 µVK^{-1}/100K) (*68*), as

shown in Fig. S11. Therefore, in the absence of quasiparticles, not only L_{eff} is significantly

suppressed from ~ $0.6L_0$ at 240K (4.5% W-doped VO$_2$) to ~ $0.1L_0$ at 341K (W-free, undoped

VO$_2$), but also S is enhanced from -12 µV/K to -18 µV/K.

While it is difficult to perform quantitative computation of Seebeck coefficient without

quasiparticles, some general expectations may be gleaned from numerical dynamic mean field

theory (DMFT) studies. The large values we have measured for S are in the same ballpark as

those obtained via DMFT in regimes where there is a linear in T dependence of S with a negative

slope, such as Fig. 1 in Ref. (*33*), Figs. 4 and 6 in Ref.(*32*), and Fig. 4 in Ref. (*69*). The behavior

in all these plots is characterized by an effectively reduced E_F in the Mott relation, as we have

found in VO$_2$, with $|S|$ ~ 0.1-0.4 k_B/e (equivalent to ~ 8.6 - 34 µV/K), significantly larger than in

conventional metals. This large Seebeck and small L_{eff} in Supplementary Materials S8 both

contribute to significantly higher S^2/L_{eff} as compared to good metals, as shown in Fig. 3C.
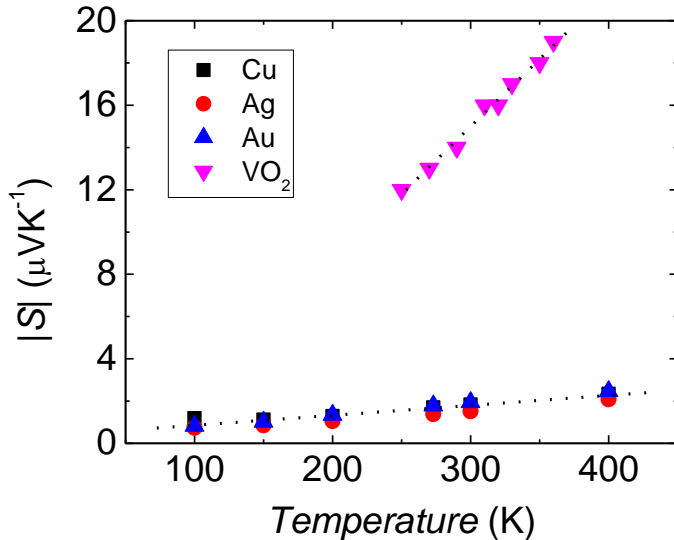
Fig. S11. Comparison of the temperature dependent Seebeck coefficient of VO$_2$ (absent

of quasi-particles) with normal, good metals (present of quasi-particles), such as Cu, Ag, and Au.

S10. Evidences of absence of quasiparticles, and decoupled charge-heat transport in VO_2 and $W_xV_{1-x}O_2$

If the material were a conventional, three-dimensional Drude metal, from the linear dependence of S on temperature (Fig. 3D), we could extract the Fermi level, E_F, from the Mott relation (which assumes the existence of quasiparticles) given by $S = \frac{\pi^2}{2e} k_B^2 \frac{T}{E_F}$. We obtain then E_F = 0.55eV, which agrees well with similar estimates in literature (*70*). This value is also in excellent agreement with that obtained from optical conductivity data (*30*) and is furthermore about half the value expected from band structure computation, as is typical for strongly correlated materials (*67*). This supports our expectation that no quasiparticles are present in VO_2 in the M phase. Assuming a three dimensional solid, $E_F = \frac{\hbar^2}{2m^*} \left(3\pi^2 n \right)^{2/3}$ for a carrier concentration of $n \sim 1 \times 10^{23}$ cm^{-3} from high quality VO_2 bulk crystals (*70*), we obtain an effective mass of $m^* = 14.3 m_0$ (where m_0 is the free electron mass). Then, using $E_F = \frac{1}{2} m^* v_F^2$, we obtain a Fermi velocity $\sqrt{\langle v_F^2 \rangle} \sim 1.16 \times 10^5$ m/s. The Fermi momentum is given by,

$$\left(p_F = m^* v_F = \hbar k_F \right)^2 = \hbar^2 \cdot \left(3\pi^2 n \right)^{2/3}$$ which gives a Fermi wavevector, $k_F = 1.44 \times 10^8$ cm^{-1}, agreeing well with $k_F \sim 1 \times 10^8$ cm^{-1} from Qazilbash *et al* (*30*). Then, using the Drude formula from our measured values of electrical conductivity ($\sigma = ne^2 \tau_{DC}/m^* = 8.1 \times 10^5$ S/m), we obtain the putative quasiparticle lifetime, $\tau_{DC} \sim \frac{1}{5} \frac{\hbar}{k_B T}$. This is a lifetime close to the "Planckian" limit $\tau_p = \frac{\hbar}{k_B T}$ (*28*), characteristic of strongly interacting metals with T-linear resistivity (*15*). Such a short lifetime cannot define long-lived quasiparticles. An independent signature of the short lifetime in metallic VO_2 comes from the fact that the M state does not exhibit a sharp Drude peak in the optical conductivity; instead, the peak is broad with a width of $> \sim k_B T$ (*29, 30*). Further,

from the optical data, the lifetime can be directly read off from the Drude-like peak at zero

frequency. In particular, from Fig. 2B in M. Qazilbash *et al.* (*30*) for the optical response in the

metallic phase VO$_2$, one obtains $\frac{1}{\tau(\omega \to 0)} = 3500$ cm^{-1}, or $\tau \sim \frac{1}{15} \frac{\hbar}{k_B T}$ (*29*). The computation of the

lifetime from DC transport, in the spirit of Bruin *et al.* (*15*), is at best an estimate given that the

Drude formula assumes the existence of quasiparticles, but its consistence with the optical

timescale is striking. Similarly, note that the Mott relation is also no longer valid in the absence

of quasiparticles. Therefore, if we naively use quasiparticle equations such as the Mott relation

for Seebeck and the Drude model for electrical conductivity, then the charge carriers would be

dissipating at timescales shorter than of of the same order of the Planckian limit (*15, 28, 71*),

which is characteristic of correlated carriers. The similar values of scattering rate from two

different experiments point to the reconciliation between the optical conductivity approach and

the separate heat and charge diffusion in our system. The DC transport quantities, however, are

not directly given in terms of this effective quasiparticle lifetime alone. The distinction between

thermal and charge transport that is revealed by the Lorenz ratio (L_{eff}/L_0) offers a unique window

into the non-quasiparticle dynamics, as it directly probes the decoupling of heat and charge

transport that would be otherwise bound together when carried by quasiparticles. Our

experiments are novel in showing that a macroscopic property such as steady state diffusion of

heat/charge under a temperature gradient is governed by non-quasiparticle physics. Similar

calculations for W-doped VO$_2$ show further decreased τ_{qp} with increasing W fraction at lower

T_{MIT}.

In the incoherent transport regime (*14*), charge and heat diffuse separately and

independently, characterized by diffusivities D_c and D_h, respectively. The respective

conductivities are then given by the standard Einstein relations $\sigma = \chi D_c$ and $\kappa_e = C D_h$. Here χ is

the charge compressibility and C the specific heat. In the absence of quasiparticles, there is no relation between the four quantities χ, D_c, C and D_h, and hence the Lorenz ratio of conductivities has no reason to take the value L_0. This is a robust, model-independent conclusion.

It should be recalled that while charge screening by Coulomb interactions means that charge does not literally diffuse in a metal, it is the unscreened charge dynamics that determines the observable conductivities. Hence the Einstein relations and other results based on unscreened diffusion still apply.

In the high temperature limit (above the bandwidth E_B, $k_B T > \sim E_B$), one expects in general that $C \sim 1/T^2$ and $\chi \sim 1/T$ with D_c and D_h constant in temperature (*14*). It follows that at high temperatures L becomes small. This general expectation is also realized by high-temperature computations using DMFT (*33*). While the data in VO$_2$ is not at such extremely high temperatures (above the bandwidth), this result indicates the tendency for L_{eff} to be small in incoherent electron fluids at high temperatures. Indeed, DMFT computations reveal that the limiting high temperature behavior typically onsets at temperatures well below the bare, un-renormalized, bandwidth (*32, 33*). While the precise temperature above which the limiting high temperature behavior will set in is difficult to predict for a given material, a qualitative prediction of the incoherent electron fluid picture is that L_{eff} should be small at high temperatures, as we have observed in VO$_2$.

As T_{MIT} is lowered with W doping, temperatures close to T_{MIT} where L_{eff} is measured are moving away from the asymptotic high-T regime. At lower temperatures, although charge and heat diffusions remain independent, one no longer expects $L_{eff} << L_0$. Instead, L_{eff} is expected to increase. For W$_x$V$_{1-x}$O$_2$, the absence of quasiparticles continues. In contrast to the increase in κ_e in W$_x$V$_{1-x}$O$_2$ (Fig.3A), σ in the M phase *decreases* with x near T_{MIT} (Fig. 3B). Thus, conventional

metallic properties for good metals, such as good charge conduction, are not recovered with the W-doping. Therefore, there is no *a priori* compelling reason for the WF law to be restored in $W_xV_{1-x}O_2$, in spite of the apparent, numerical recovery of L_{eff} toward L_0 (Fig. 3C).

Modest deviations of L_{eff} from L_0, as much as $\sim 0.4 < L_{eff}/L_0 < \sim 3.6$, have been reported in several metals and degenerately doped semiconductors (*72*). These deviations occur when the mean free path of electrical transport becomes unequal to that of electronic thermal transport. This may arise from inelastic scattering events such as collisions between electrons and optical phonons, which are in contrast to elastic scattering of electrons by impurities or boundaries. In the $W_xV_{1-x}O_2$ samples, however, as stated in the main text, the average W-W distance is estimated to be ~ 1 nm. This estimation was made with volumetric spacing for the W-doped samples. For 2.1%, 2.6%, and 4.5% W-doping, it is estimated to be 1.1 nm, 1.1 nm, and 0.9 nm, respectively. If using the Drude model to estimate the mean free path of electrons, given by $l_e = v_F \cdot \tau \sim 0.5$ nm, all these W-W distances are longer than this estimated mean free path. Our value of the mean free path is in close agreement with literature value (~ 0.3 nm), and the difference is caused by the variation of the Fermi wavevector ($k_F \sim 1 \times 10^8$ cm^{-1} in Qazilbash *et al* (*30*)) as compared to 1.44×10^8 cm^{-1} in our estimation above. Such a relatively large value of W-W spacing and the small change in it are unlikely to bring elastic scattering to a dominant role in the electronic transport. However, this does not completely rule out a possible contribution of elastic scattering by W doping to the rise in Lorenz number. Based on the discussion above and the persistence of the incoherent, non-quasiparticle transport, therefore, we can only conclude that the rise observed in L_{eff} upon W doping likely originates from both: (a) the incoherent, non-quasiparticle transport electrodynamics, in which the ratio of the temperature dependence of the charge susceptibility and the electronic specific heat determines L_{eff}, as well as (b) increased

elastic scattering by the W dopants. It is worth emphasizing again that even with the highest W-doping of 4.5%, charge and heat still diffuse independently with the absence of quasiparticles, evidenced by the collapse of the Seebeck for different W-doping levels (Fig. 3D) and the increasingly high resistivity.

The measured value of S^2/L_{eff} also rules out an alternative mechanism giving a similarly small L_{eff}. If a metal enters a specific type of quasi-hydrodynamic regime dominated by momentum relaxation, then a small L_{eff} follows from a kinematic cancellation arising due to the electric open-circuit boundary condition under which κ_{tot} is measured (4). However, this cancellation requires $S^2/L_{eff} \gg 1$, in contradiction with the measurements (Table S3). This regime furthermore predicts a sharp Drude peak, in contrast with the broad peak observed in VO_2 (29, 30).

The recent experimental demonstration of violation of the WF law in semi-metallic graphene (12) indeed occurs in such a quasi-hydrodynamic, coherent charge transport regime, in which momentum is long-lived. However, due to the low density of charge carriers close to the particle-hole symmetric point, in that system, momentum transports heat more efficiently than charge. One therefore instead expects a large $L_{eff} \gg L_0$ in semi-metal hydrodynamics, as observed in Ref. (12). Incoherent transport in metallic VO_2 is markedly different, since momentum deteriorates rapidly, see previous paragraphs and Ref.(14). This distinct, incoherent dynamics leads to the $L_{eff} \ll L_0$ at high temperatures that we have observed.

material	S (μV/K)	L_{eff}/L_0	S^2/L_{eff}
VO_2	-18	1.1×10^{-1}	1.2×10^{-1}
$W_{0.021}V_{0.979}O_2$	-15	2.6×10^{-1}	3.6×10^{-2}

W$_{0.045}$V$_{0.955}$O$_2$	-11	5.9×10^{-1}	8.4×10^{-3}
Cu	1.8	1.0	1.3×10^{-4}

Table S3. Seebeck coefficient S, effective Lorenz number L_{eff}, and electronic figure of merit S^2/L_{eff} of metallic W$_x$V$_{1-x}$O$_2$ nanobeams near their T_{MIT}. The parameters for Cu (*73*) are at room temperature. For most conventional metals (*74*), their S^2/L_{eff} ranges from values as small as that of Cu (~ 10^{-4}) to up to ~ 10^{-3}.